Space Weather

RESEARCH ARTICLE
10.1029/2018SW002098

Special Section:
Scientific Challenges of Space Weather Forecasting Including Extremes

**Key Points:**
- Solar magnetic fields are projected outward through the interplanetary medium to provide a daily prediction and forecast of GSM $B_z$
- The GSM $B_z$ field decreases we predict are shown to provide a forecast of minor to moderate geomagnetic storm activity
- Our predicted GSM $B_z$ amplitude variations are shown to maximize near the times of the vernal and autumnal equinoxes

**Correspondence to:**
B. V. Jackson,
bvjackson@ucsd.edu

**Citation:**
Jackson, B. V., Yu, H.-S., Buffington, A., Hick, P. P., Tokumaru, M., Fujiki, K., et al. (2019). A daily determination of $B_Z$ using the Russell-McPherron effect to forecast geomagnetic activity. *Space Weather*, *17*, 639–652. https://doi.org/10.1029/2018SW002098

Received 8 OCT 2018
Accepted 18 MAR 2019
Accepted article online 03 APR 2019
Published online 25 APR 2019



# A Daily Determination of $B_Z$ Using the Russell-McPherron Effect to Forecast Geomagnetic Activity

**B. V. Jackson[1], H.-S. Yu[1], A. Buffington[1], P. P. Hick[1], M. Tokumaru[2], K. Fujiki[2], J. Kim[3], and J. Yun[4]**

[1]Center for Astrophysics and Space Sciences, University of California at San Diego, La Jolla, CA, USA, [2]Institute for Space-Earth Environmental Research, Nagoya University, Nagoya, Aichi, Japan, [3]Korean Space Weather Center, National Radio Research Agency, Gwideok-ro, Hallim-eup, Jeju-si, Jeju-do, South Korea, [4]SELab, Seoul, South Korea

**Abstract** Since the middle of the last decade, UCSD has incorporated magnetic field data in its Institute for Space-Earth Environmental Research interplanetary scintillation tomographic analysis. These data are extrapolated upward from the solar surface using the Current Sheet Source Surface model (Zhao & Hoeksema, 1995, https://doi.org/10.1029/94JA02266) to provide predictions of the interplanetary field in RTN coordinates. Over the years this technique has become ever more sophisticated, and allows different types of magnetogram data (SOLIS, Global Oscillation Network Group, etc.,) to be incorporated in the field extrapolations. At Earth, these fields can be displayed in a variety of ways, including Geocentric Solar Magnetospheric (GSM) $B_x$, $B_y$, and $B_z$ coordinates. Displayed daily, the Current Sheet Source Surface model-derived GSM $B_z$ shows a significant positive correlation with the low-resolution (few day variation) in situ measurements of the $B_z$ field. The nano-Tesla variations of $B_z$ maximize in spring and fall as Russell and McPherron (1973, https://doi.org/10.1029/JA078i001p00092) have shown. More significantly, we find that the daily variations are correlated with geomagnetic Kp and Dst index variations, and that a decrease from positive to negative $B_z$ has a high correlation with minor-to-moderate geomagnetic storm activity, as defined by NOAA Space Weather Prediction Center planetary Kp values. Here we provide an 11-year study of the predicted $B_z$ field, from the extrapolation of the Global Oscillation Network Group-magnetograms. We provide a skill-score analysis of the technique's geomagnetic storm prediction capability, which allows forecasts of moderate enhanced geomagnetic storm activity. UCSD and the Korean Space Weather Center currently operate a website that predicts this low-resolution GSM $B_z$ field component variation several days in advance.

## 1. Introduction

Earlier articles (Jackson et al., 2010, 2011, 2013) show the utility of using interplanetary scintillation (IPS) analysis to provide the heliospheric plasma parameters velocity and density at Earth, using the UCSD 3-D reconstruction technique. In these analyses, Institute for Space-Earth Environmental Research (ISEE), Japan (Kojima & Kakinuma, 1987; Tokumaru, 2013; Tokumaru et al., 2011), IPS is generally used as a remotely sensed data source since they are available regularly online at ftp://ftp.stelab.nagoya-u.ac.jp/pub/vlist/rt/ and updated early in the day following their being obtained. This allows UCSD to provide forecasts of conditions in the interplanetary medium a few days into the future because the IPS observations are obtained from closer to the Sun than Earth, and usually heliospheric structures take about 4 days to travel to 1 AU.

National Solar Observatory Global Oscillation Network Group (GONG) observations (http://gong.nso.edu/data/magmap/) provide solar surface magnetic field data to the Current Sheet Source Surface (CSSS) model (Zhao & Hoeksema, 1995) for input to the 3-D reconstruction analysis (see Dunn et al., 2005). These fields vary rather smoothly even though they are currently provided as a new source surface with a 6-hr cadence to the UCSD 3-D reconstructions (see section 2.2) and are unaveraged in transit or at Earth for comparison with in situ measurements. As discussed in Jackson et al. (2016), and known to be necessary to make field strengths match in situ measurements (e.g., Linker et al., 2017), GONG data are multiplied by a factor of two from the original surface fields in order to provide a more accurate amplitude comparison at Earth. In the usual CSSS modeling effort, we call "open field" in Jackson et al. (2016), there are only radial fields present on the inner source surface. Using the Parker (1958) solar wind equations, this field is extrapolated outward in the UCSD 3-D reconstructions as a “frozen in” field that conserves the timing and interactions present in the UCSD time-dependent kinematic model. In this formulization using heliographic coordinates, there are only radial and tangential fields (RTN in heliographic radial, tangential, and normal coordinates) present; the north-south (normal) field is zero. Jackson et al. (2016) provide a comprehensive analysis of how well these field predictions compare with Advanced Composition Explorer (ACE; Stone et al., 1998), or Wind (Ogilvie & Parks, 1996) in situ measurements over the 10-year period of available GONG data.

The determination of magnetic field direction and strength is an important prediction goal in heliospheric physics because magnetic field strengths and directions are one way that the Sun interacts with nearby planetary bodies. At Earth a southward field in Geocentric Solar Magnetospheric (GSM) coordinates can couple with Earth's geomagnetic field (e.g., Kamide et al., 1997; Russell, 2001) to provide geomagnetic activity. Geomagnetic prediction models generally attempt to extrapolate north-south fields into the interplanetary medium associated with Coronal Mass Ejections (CMEs) since these are well-known progenitors of the largest geomagnetic storms (e.g., MacNeice et al., 2018). However, for minor and moderate storms there are generally no known associated CMEs observed in situ (e.g., see Choi et al., 2017). In fact, much substorm activity is generally thought associated with corotating heliospheric structures (Tsurutani et al., 2006).

This article shows for the first time that a large portion of this storm activity can be associated with the daily cadence presentation of southward turning magnetic field in GSM coordinates that is accompanied by the tangential field direction in RTN coordinates. Although this has been noted before as a weakly present variation in geomagnetic activity known as the Russell-McPherron effect (Russell & McPherron, 1973), we show that the UCSD analysis of the $B_z$ conversion of the tangential RTN component daily provides a reasonable prediction of background $B_z$ values, and also a good forecast of minor (Kp of 5) to moderate (Kp of 6) and greater storm activity several days into the future using our 3-D reconstruction technique.

Section 2 of the present article provides a further accounting of how GONG data sets are extrapolated to 1 AU where they are converted to GSM coordinates and compared with ACE in situ measurements. Section 3 details the 11-year study that correlates the $B_x$, $B_y$, and $B_z$ GSM fields near Earth from our GONG extrapolations with ACE in situ magnetic fields. Section 4 is a similar 11-year comparison analysis of GSM $B_z$ from our extrapolated values and ACE in situ measurements compared with Dst downloaded from the OMNI website. Section 5 discusses these results in terms of the Russell McPherron effect. Section 6 shows an example where the values of positive Kp have been forecast, and includes a skill-score determination of predicted $B_z$ decreases with Kp index. We conclude in section 7.

## 2. Tomographic Analysis and Field Extrapolation Using a Sample Data Set

We note here a distinction between predictions and forecasts. In this article predictions are the ability to extrapolate remotely sensed data on from the Sun and inner heliosphere to provide modeled values that are checked by in situ measurements at the current time. Forecasts are the ability to provide warning of an impending event. Predictions can be available using archived data sets while true forecasts are present only in real time without knowledge of the eventual outcome. Both are available using the IPS analyses and will be discussed in the following sections. Although the UCSD analysis makes a forecast of impending southward $B_z$ values, these are only one of many diagnostics that large space weather institutions have available to provide a final version of what will actually occur.

### 2.1. UCSD Plasma Velocity and Density Predictions and Forecasts

IPS observations began in earnest in the early 1960s, primarily with work in Cambridge, England, by Hewish et al. (1964); it was clear from that time onward that this allowed a remotely sensed depiction of the inner heliosphere (Ananthakrishnan et al., 1980; Behannon et al., 1991; Gapper et al., 1982; Hewish & Bravo, 1986; Houminer, 1971). However, it was not until computer assisted tomography (CAT) was introduced (Jackson et al., 1998; Kojima et al., 1998) that heliospheric structures could be readily used to predict conditions at 1 AU and globally throughout the inner heliosphere. IPS observations from ISEE, Japan—formerly named the Solar-Terrestrial Environment Laboratory—have been used for space weather predictions and forecasts since early in this century (see Jackson et al., 2011; Tokumaru, 2013, for reviews).

10.1029/2018SW002098

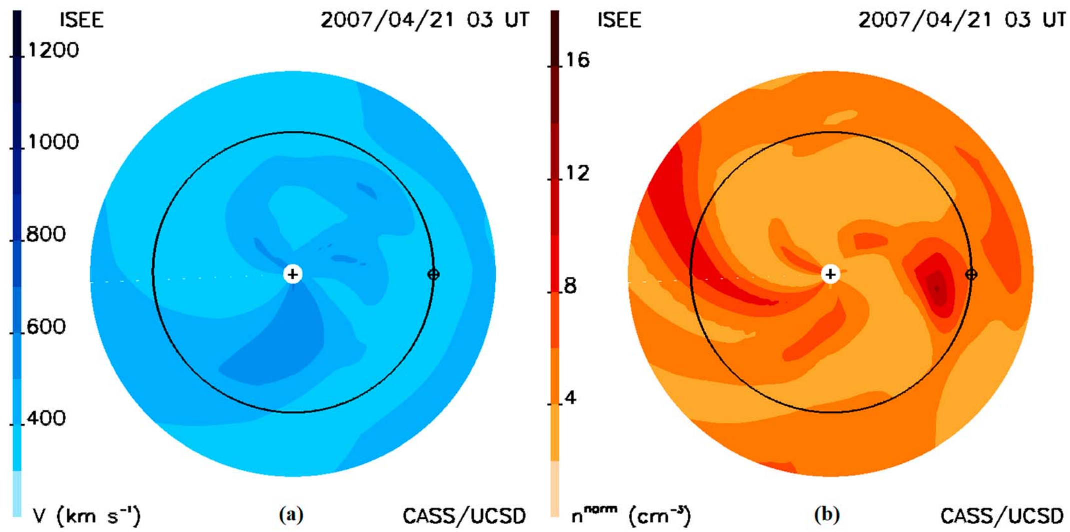


**Figure 1.** Sample of the UCSD volumetric analysis shown here as ecliptic cuts through the 3-D reconstructed volume from 15 Rs out to 1.5 AU. The Sun is in the center of each plot with the Earth shown on its orbit to the right. A contour scale is given to the left. (a) Radial velocity. (b) Density given in protons cm$^{-3}$. An $r^{-2}$ falloff has been removed from the density to normalize values to 1 AU. ISEE = Institute for Space-Earth Environmental Research.

Both the UCSD and ISEE iteratively fit IPS observations of velocity perpendicular to the line of sight. However, unlike the ISEE CAT program, the kinematic program used at UCSD provides a time-dependent analysis that fits IPS scintillation-level as a density proxy and conserves mass and mass flux from a lower boundary at 15 Rs (Jackson & Hick, 2005; Jackson et al., 2003, 2008, 2010, 2012, 2013). The time-dependent aspect of the UCSD CAT program allows both CMEs and corotating structures to be reproduced. Heliospheric features first viewed close to the Sun can be followed until they pass to the edge of the reconstructed volume that is generally extended to 3 AU. Use of the full IPS data set is an obvious prediction of event processes at Earth. An archival analysis of these time-dependent reconstructions has been available on the UCSD website: http://ips.ucsd.edu from the year 2000. Since early in this century, the NASA Goddard Community Coordinated Modeling Center has also maintained a “runs on request” version of UCSD prediction analysis at their website (https://ccmc.gsfc.nasa.gov/requests/requests.php). Jian et al. (2015, 2016) have compared the IPS results from the IPS prediction modeling and have as good or a better correlation with in situ measurements than other heliospheric models extant at the Community Coordinated Modeling Center over the seven Carrington rotations studied in 2007. Since spring 2013 a near real-time forecast analysis of plasma parameters density and velocity has also been used at http://iswa.ccmc.gsfc.nasa.gov (MacNeice et al., 2018).

IPS results are normalized and compared with a variety of different in situ measurements including velocities and densities from the ACE, Solar Wind Electron Proton Alpha Monitor (SWEPAM) (McComas et al., 1998), and densities measured from ACE or from the Charge, ELement, Isotope Analysis System (CELIAS) proton monitor (Hovestadt et al., 1995) onboard the SOlar and Heliospheric Observatory (SOHO) spacecraft (Domingo et al., 1995). Even more recently NOAA's DSCOVR satellite (https://www.nesdis.noaa.gov/content/dscovr-deep-space-climate-observatory) in situ measurements have been incorporated in near real-time comparisons.

Figures 1 and 2 are samples of the IPS respective volumetric velocity and density analysis from the UCSD archival website using 3-D reconstructions that have resolutions of 20° × 20° in latitude and longitude, and a 1-day time cadence, and are fairly typical for this period and time of year (see ftp://cass185.ucsd.edu/data/IPS_archival_data/). Because speeds remain generally constant within a factor of two in the heliosphere, and material expands outward as a spherical shell, ecliptic cuts through the reconstructed density, as in Figure 1b, have an $r^{-2}$ falloff removed, normalized to 1 AU to best display structures as they move outward from the Sun. In situ densities and velocities obtained from NOAA are smoothed in time with a 1-day moving boxcar mean to make them commensurate with the low-resolution IPS 3-D reconstruction

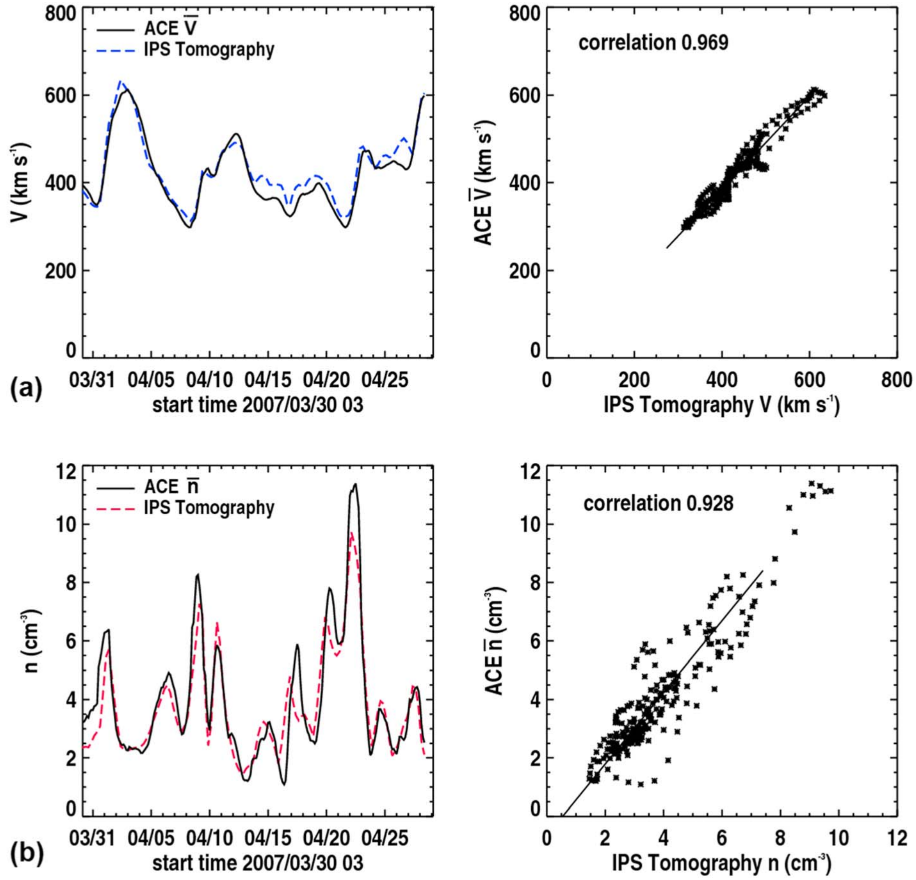


**Figure 2.** Time series from the IPS 3-D reconstructions (dashed lines) compared with ACE Solar Wind Electron Proton Alpha Monitor Level 0 measurements over the same Carrington rotation 2055 time period. The in situ measurements have been smoothed by a 1-day boxcar filter to provide a signal commensurate with the 1-day cadence of the tomographic analysis. A Pearson's "$R$" correlation coefficient is given in the right panel of the time series. The density structure about to reach Earth in Figure 1b appears here as a small increase in velocity on 23 April 2007 (a) that follows an increase in density (b). ACE = Advanced Composition Explorer; IPS = interplanetary scintillation.

analysis. This averaging matches the approximate temporal and distance resolutions available in the tomographic analysis near Earth (see Jackson et al., 2008).

### 2.2. UCSD Extrapolation of CSSS Fields and the Prediction of GSM $B_z$

The 3-D reconstruction of the solar wind velocity in the UCSD time-dependent analysis is used to forward-model the Zhao and Hoeksema (1995) CSSS RTN magnetic field, extending it out to the edge of the global boundary considered by the IPS analysis. As previously mentioned, more detailed descriptions are found in Dunn et al. (2005) and in Jackson et al. (2012, 2016). Even though GONG synoptic maps are currently updated with a 6-hr cadence in the UCSD time-dependent tomography, our analysis essentially provides only background solar wind component fields. The reason for this, as discussed in Dunn et al. (2005), is that rapidly changing transient currents and their associated fields, such as those from CMEs in the corona and inner heliosphere, currently are not observable on a regular basis. We here project RTN coordinate radial and tangential fields outward using the Parker (1958) postulation (see Figure 3; also in Dunn et al., 2005, and Jackson et al., 2016). Here, $B_r$, $B_\phi$, and $B_\theta$ are, respectively, the radial, tangential, and normal components of the field that vary with radius ($r$) relative to the 1 AU value ($r_0$), velocity ($V$), and solar rotation ($\omega$), and this formulization has $B_\theta$ equal to zero. However, since 2005 until late 2016, we only compared to ACE measurements in RTN and we did not convert our values to GSM because we assumed that the relatively small $B_z$ component impressed from $B_\phi$ would not give a statistically significant result.

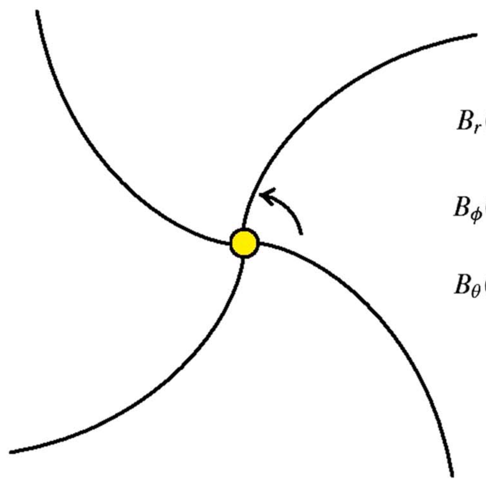

$$B_r(r, \phi, \theta) = B(r_0, \phi_0, \theta_0)\left(\frac{r_0}{r}\right)^2$$

$$B_\phi(r, \phi, \theta) = -B(r)\left(\frac{\omega r_0 \sin(\theta)}{V}\right)\left(\frac{r_0}{r}\right)$$

$$B_\theta(r, \phi, \theta) = 0$$

**Figure 3.** In the heliosphere beyond the Current Sheet Source Surface model source surface, the rotating Sun provides a spiral field that approximately follows the equations given above in RTN coordinates as structures flow approximately radially outward from the source surface near the Sun. The spiral field that gives rise to both a radial and tangential field component in RTN coordinates provides no field normal to the solar equatorial plane.

Although solar rotation provides no normal field perpendicular to the solar equatorial plane, GSM coordinates are defined in a plane perpendicular to the solar radial direction and the $B_z$ field is parallel to the projection of the solar geomagnetic axis in that plane. In both the spring and fall of a year the tangential field in RTN coordinates has a maximum vector component directed along the $B_z$ field component; this field component can couple with the Earth's field component, and as shown by Russell and McPherron (1973), correlates with enhanced geomagnetic activity in the spring and fall. To show this in a graphical way, Figure 4 depicts the Earth's position at the autumnal equinox as an observer would view Earth and the eclipsed Sun from slightly beyond 1 AU. The ecliptic is shown as the straight horizontal line; the heliographic equator as an elongated ellipse at the time of the equinox. The Earth is shown with an arrow depicting the direction of the north geographic pole that has a 23° tilt relative to the ecliptic plane. This tilt is slightly greater than 23° relative to the heliospheric tangential component of field at this time. The average daily geomagnetic field with a daily wobble is aligned approximately with the geographic polar axis. The GSM coordinate system is defined by a plane that is perpendicular to the radial from the Sun and is in the plane of the paper in this figure. UCSD extrapolates the radial and tangential magnetic fields in RTN coordinates. In RTN coordinates $B_r$ is antiparallel to $B_x$ in GSM coordinates, but the difference between the Earth's polar field direction and the heliographic equator provides a small field component that is either in, or opposite to, the direction of the Earth's polar field. The inset to the lower right gives the ±direction ($B_t$) of the RTN tangential field component at Earth at this time; the average daily geomagnetic field component (G) is also shown. Plotted as a daily average, or more frequently, this G field is the component that can couple to the Earth's polar field.

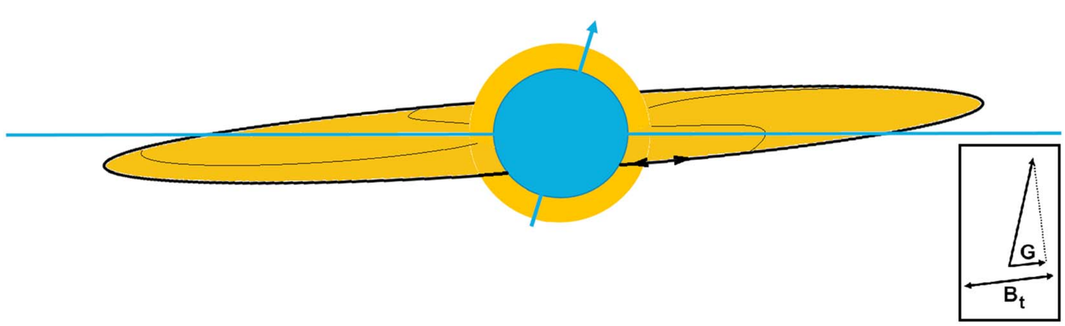


**Figure 4.** Geocentric Solar Magnetospheric coordinate vector map at the autumnal equinox. The Earth in blue is depicted in front of the Sun. The inset to the right gives the direction of the tangential field relative to the average daily geomagnetic field component.

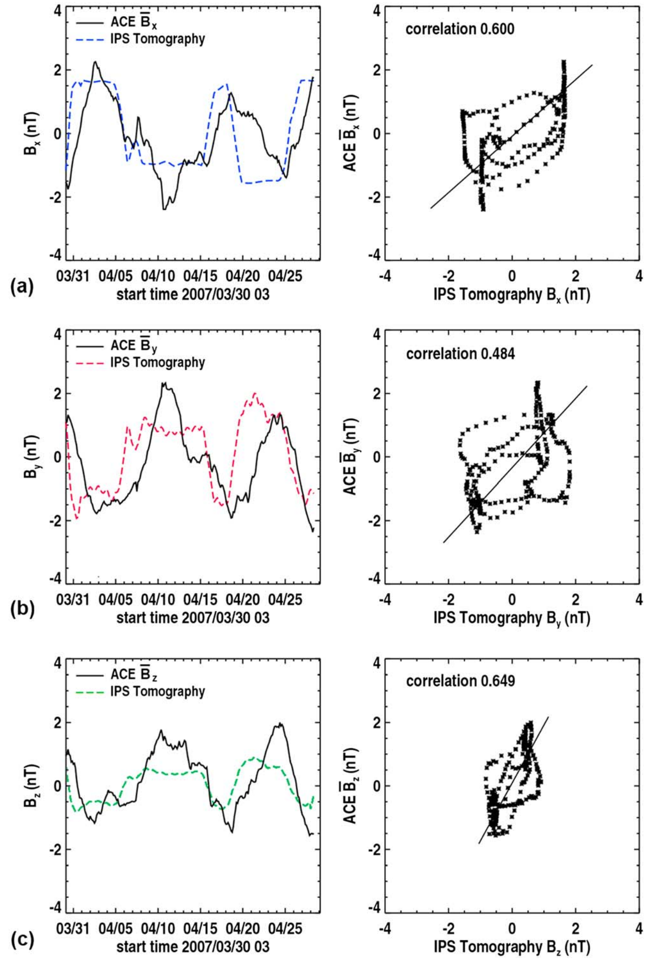


**Figure 5.** Time series from the Current Sheet Source Surface modeling and IPS 3-D reconstruction extrapolations of Global Oscillation Network Group data (dashed lines) converted to Geocentric Solar Magnetospheric coordinates at Earth compared with ACE magnetometer measurements in Geocentric Solar Magnetosphere over the same Carrington rotation 2055 period. The in situ measurements have been smoothed by a 3-day boxcar filter as indicated in the upper left hand corner of each of the first panels and on the vertical axis on the right panels above to provide a signal commensurate with the smoothed values from the Current Sheet Source Surface tomography modeling. (a) $B_x$, (b) $B_y$, (c) $B_z$. ACE = Advanced Composition Explorer; IPS = interplanetary scintillation.

The accurate velocity and timing from the IPS tomographic velocities and relatively good correlations using the UCSD kinematic modeling allow us to take the forward modeled RTN coordinate fields one step farther and provide GSM $B_x$, $B_y$, and $B_z$ fields modeled daily.

## 3. Correlations Between IPS GONG Extrapolations and GSM $B_x$, $B_y$, and $B_z$

Sample plots of the IPS CSSS magnetic field model extrapolations from the tomographic source surface at 15 Rs are shown in Figure 5 for Carrington rotation 2055. These are converted to GSM coordinates and superimposed over the corresponding ACE fields. Although the GONG synoptic maps are currently refreshed approximately every 6 hr, the changes in extrapolated field are not as great as either the densities or velocities at 1.0 AU, and thus to match these fields we have averaged the ACE in situ measurements given by NOAA as 1-hr averages with a 3-day boxcar filter. The reason for this averaging interval is explored more fully in Jackson et al. (2016) and has to do with factors that include the smoothing and outages present in the GONG data that provides input to the CSSS model, the CSSS model itself, and potential solar wind nonradial flow that is not supported by the UCSD kinematic 3-D reconstruction model. The Pearson's $R$ correlation between the time series is shown to the right above each panel. Clearly there is a significant correlation between each time series, even for the GSM $B_z$ component. We do not plot $p$ values (or the statistical significance of these results), but these can be determined for each comparison simply enough by assuming that there are a given number of independent values throughout the Carrington rotation for each correlation coefficient. Although there are variations of shorter length in our 3-day boxcar averages in a Carrington rotation (27 days in length), in the worst case, a 3-day boxcar average implies nine independent variables are present for each Carrington rotation correlation. An $R$ correlation of 0.8 gives about one chance in 100 of having a null hypothesis, and with many of these $p$ values at different times throughout the 11-year period, a null hypothesis for the ensemble of rotations is extremely unlikely (also see section 4).

As in Jackson et al. (2016) we provide these correlations from the beginning of the GONG data set. Unlike the former analysis, we have provided correlations with tomographic resolutions that are slightly less well resolved (with a 20° × 20° latitude and longitude resolution and a 1-day temporal cadence) from 2006 until nearly the end of 2017. Figures 6a and 6b give the results of the correlations of $B_x$ and $B_y$ for each Carrington rotation studied. With few exceptions every rotation throughout the 11-year period shows a high positive correlation between the field extrapolated to Earth by our CSSS modeling technique and the NOAA-provided GSM measured coordinate. A significant positive correlation is also generally present for most Carrington rotations between our extrapolated CSSS modeled Bz value and the GSM Bz component (Figure 6c) throughout the 11-year period. Here we have culled the comparison data set somewhat to allow only those Carrington maps with amplitude variations larger than 0.25 nT to be used in the analysis.

Because of UCSD computer memory limitations, the time-dependent tomography can only be calculated for a few Carrington rotations at a time. In addition, the IPS analyses have not been continuous through the years prior to 2010 because of array closure due to winter mountain snow in Japan. Additionally, the array system is sometimes closed for week long intervals for maintenance. Thus, we have not previously provided a correlation of the whole time series throughout the 11-year period, and have only assumed that the Carrington rotation end effects in our analysis do not influence the outcome. As a check on this, however,

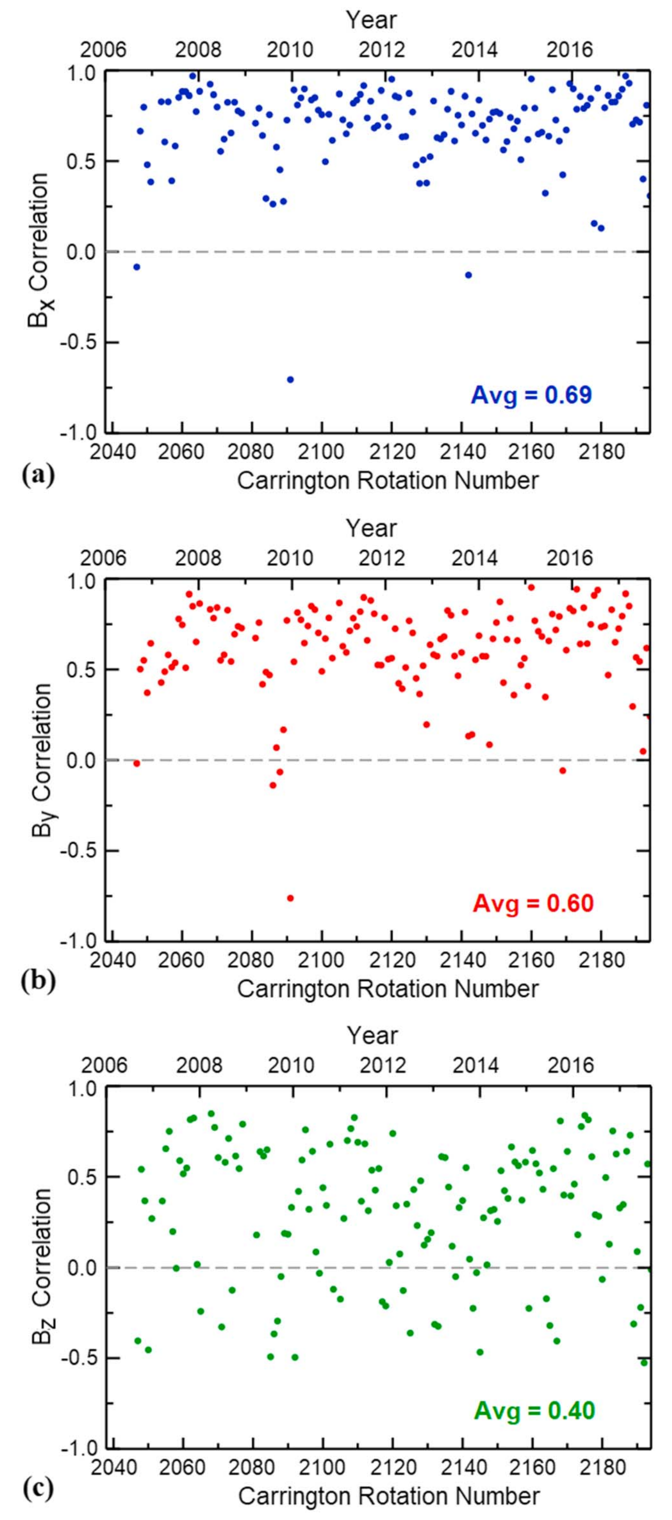


**Figure 6.** Eleven-year study of Pearson's *R* correlations for the Current Sheet Source Surface model Global Oscillation Network Group extrapolated Geocentric Solar Magnetospheric field component correlations compared with Advanced Composition Explorer in situ observations per Carrington rotation (a) $B_X$, (b) $B_Y$, (c) $B_Z$—correlations with extrapolated amplitude variations >0.25 nT only.

we have joined each time series in the analysis, and have calculated correlations where GSM observations exist from both ACE measurements and the IPS data for each component from 8 March 2009 through to 10 July 2018. For this more than 9-year interval, only 2% of the comparison times are missing, The correlation comparisons over this interval are, respectively, 0.685, 0.636, and 0.382 for $B_x$, $B_y$, and $B_z$, confirming that end effects from our individual Carrington rotation analyses have little significance for the Figure 6 average correlation outcomes. This is in spite of the fact that including the low amplitude variations for the continuous time series correlation adds noise to the comparison in the more restricted data set of Figure 6c.

## 4. GSM $B_z$ Correlations With Dst and Kp Over the 11-Years of GONG Data

In this section, our CSSS extrapolated fields converted to GSM for Carrington rotation 2055 are correlated with Dst. In these analyses Dst has been averaged with a 3-day boxcar to be commensurate with the approximate averaging present over the Carrington rotation available from our modeled values of $B_z$. In the example plotted in Figure 7 we see a positive correlation with Dst that is as high as the comparison between our extrapolated value of $B_z$ and that measured by ACE! This comparison takes more explanation in its presentation. Dst is a geomagnetic storm-time index developed to specify the severity of geomagnetic activity; the largest Dst variations can appear over a period of much less than a 3-day interval and these are generally present in the data we access through the OMNI website at http://wdc.kugi.kyoto-u.ac.jp/dst_final/index.html where this index is given at 1-hr intervals. Our boxcar averaging decreases the amplitude of the 1-hr measurements from this website. In the example shown in Figure 7, the largest Dst decrease (−63) in 1-hr measurements from the OMNI website during this Carrington rotation occurred suddenly at 9 UT 1 April, and recovered gradually over the next few days until it became positive on 8 April. The next largest Dst decrease during this Carrington rotation period in the 1-hr data occurs at 1 UT 28 April (−42) again beginning abruptly a few hours before this but lasting for over the following 6 days. Both the positive and negative $B_z$ decreases somewhat precede our plotted low-resolution Dst indices. Dst index gives a measure of the ring current around Earth and is used to assess the severity of geomagnetic storms. The actual measurement given at the Kyoto website are derived from the horizontal component of the geomagnetic field that approximates the uniform magnetic field parallel to the geomagnetic dipole axis and directed southward. Thus, our $B_z$ variations that couple with Earth's geomagnetic field should have a similarity to the derived Dst index with a lag impressed if by nothing else than the abrupt onset and more gradual increase generally presented in Dst variations. Since the UCSD 3-D extrapolation of fields gives little indication of the short-term transient field variations in the corona, and no indication of the mechanics of the rapid changes of the ring current, especially at the onset of large geomagnetic storms, the correlations in the few-day resolution data per Carrington rotation that we find seem reasonable to us. We note that our value of $B_z$ needs to be multiplied by a factor of ~13 to give variations similar to those of our averaged Dst index magnitude.

Following, we now show the comparisons of our extrapolated CSSS model values of field converted to GSM $B_z$ over the more than 11-year period of

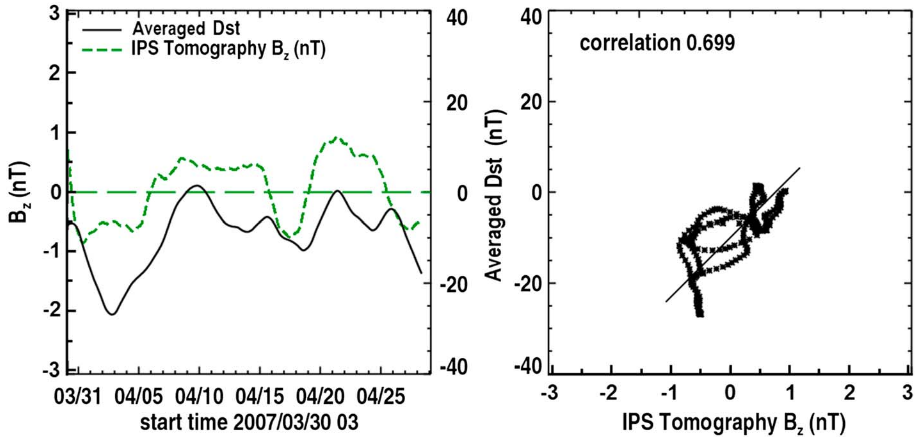


**Figure 7.** Time series from the Current Sheet Source Surface modeling and IPS 3-D reconstruction extrapolations of Global Oscillation Network Group data converted to Geocentric Solar Magnetospheric coordinates at Earth (dashed lines) compared with a 3-day boxcar averaged Dst for the Carrington rotation 2055 period. IPS = interplanetary scintillation.

GONG data. Figure 8 gives the correlation comparison with Dst. Here, while most of the comparisons show correlations of the sign expected, and while the correlations with Dst can be as high as 0.8 for a given Carrington rotation, there are notable exceptions and overall the correlations are not that good as those of the values of extrapolated flux converted to GSM $B_z$ compared with ACE. Even so the ensemble of 97 points provides a $p$ value for these correlations that gives one chance in ~$10^{12}$ that a null result is possible. There is also a general trend shown; there are more negative correlations in the middle of the 11-year period studied than at either end. Since the maximum of sunspot cycle 24 is from the middle of the year 2011 until the beginning of 2015 this is a good indication that the correlations observed are best during periods of low solar activity. The nearly continuous time period correlation from 2009 to 2018 of Bz with Dst is 0.220 and as for Figure 6c, again confirms that even with added noise, the correlations over the nearly 9-year interval are positive and have approximately the same significance as the more restricted data set of Figure 8. NOAA's planetary Kp index determinations compared with $B_z$ give similar results for the 11-year period studied with corresponding negative correlations ($-B_z$ provides a positive Kp).

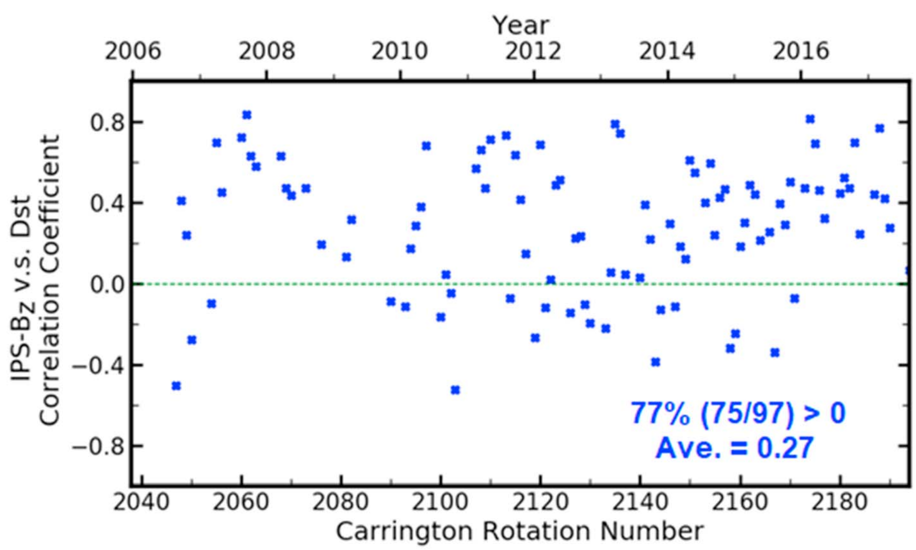


**Figure 8.** Eleven-year study of Pearson's $R$ correlations for the Current Sheet Source Surface model Global Oscillation Network Group Geocentric Solar Magnetospheric $B_z$ field component analysis compared with the averaged Dst. Only Carrington rotation correlations with extrapolated amplitude variations >0.25 nT are used. IPS = interplanetary scintillation.

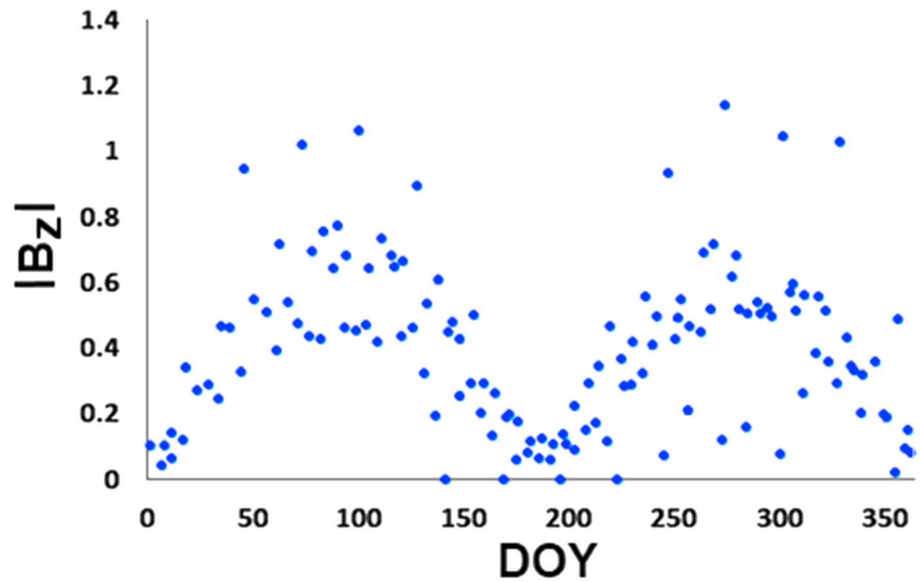


**Figure 9.** Annual yearly amplitude excursion of the extrapolated Current Sheet Source Surface model $B_z$ field component. DOY = day of year.

## 5. The $B_z$ Analysis as a Russell-McPherron Effect

The $B_x$ radial field component mapped in Figure 6a is essentially the same as that mapped in the Figure 6 open field analysis in Jackson et al. (2016). The correlation average over more than 11 years in this study is 0.69 whereas in the earlier 10-year study this average was 0.65. Clearly the $20° \times 20°$ latitude and longitude spatial and 1-day time cadence resolution that is poorer for this analysis does not have much effect in the outcome for mapping this field component. The greater than 11-year correlation average value of the $B_y$ field of 0.60 (Figure 6b) is similar, but not exactly the same as the 0.56 average of the GONG field *tangential* component value given in Figure 8 of the earlier article. The average correlation of 0.40 in Figure 6c for this 11-year study of the $B_z$ field for Carrington Rotations with field amplitude excursions greater than 0.25 nT is truly unique.

To show that the effect observed is primarily due to the coupling of the RTN tangential field with Earth's magnetic field, as noted by Russell and McPherron (1973), we plot for each Carrington rotation the amplitude excursions of our $B_z$ modeled values over this period folded into a 1-year plot in Figure 9. This shows that at the beginning of the year and in the middle of the year when there is no daily average crossed field component as indicated in Figure 4, there is little observed Carrington Rotation $B_z$ excursion amplitude from this effect, and thus no component of the extrapolated field that can couple with the geomagnetic field.

Of course, other coronal and heliospheric changes and interactions are present in the background solar wind that yield heliospheric north-south $B_z$ fields that can couple with the geomagnetic field directly; we do not explore these except we here merely note that they exist, and also that they can provide an even greater range of field excursions than the present effect. The highly variable transient fields associated with CMEs are well known, and these can give a far larger excursion. The fact that there is not as good a correlation in this analysis during solar maximum is undoubtedly partly due to the many transient fields in the inner heliosphere present including those from CMEs. However, CME field excursions seldom last for more than a day, whereas a southward field seen here can persist for many days, and we suspect these have the potential to enhance storm activity over a longer time interval with associated additional decreases in the $B_z$ field.

## 6. $B_z$ Forecast Analysis and Kp Examples of Applicability

In forecasting, IPS observations of all outgoing structures throughout the viewing volume to 3 AU are obviously not available in real time before those that are Earthward-directed arrive. Thus, there is not as much IPS data available to provide a complete description for the UCSD 3-D reconstructions in a forecast

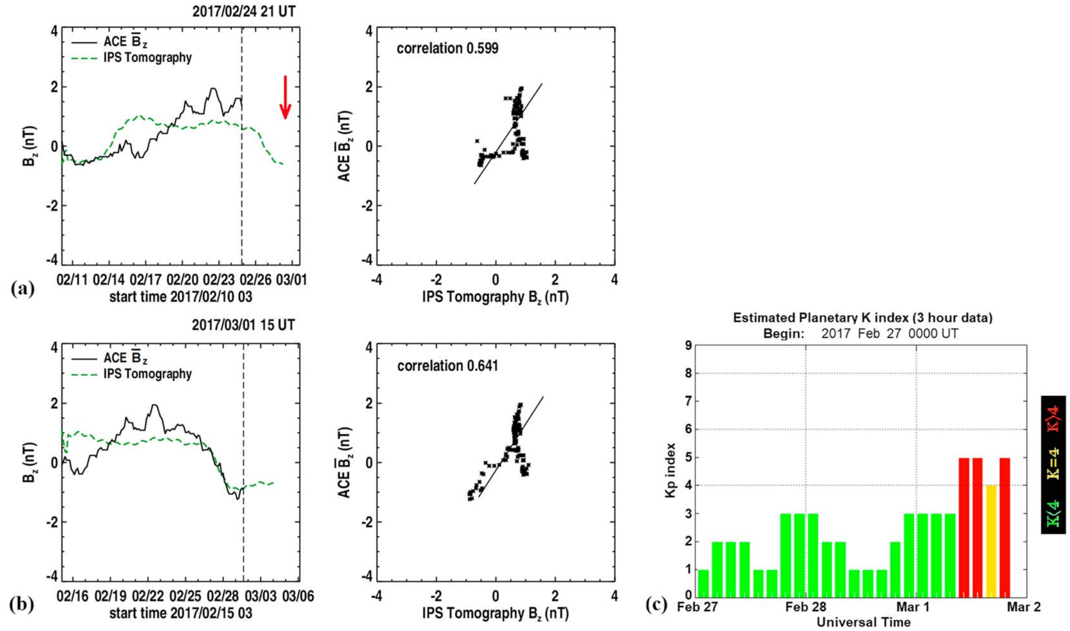


**Figure 10.** Example of an impending $-B_z$ change on the UCSD website, and the subsequent associated geomagnetic activity. A dashed vertical line is given at the time the forecast is presented on the UCSD website. A projection provided several days into the future shows forecast changes expected to occur in (a). The forecast $B_z$ component changes have tracked the Geocentric Solar Magnetospheric $B_z$ 3-day averaged values on the NOAA website well in (b), and on 1 March 2017 the NOAA planetary index increased as shown (c). ACE = Advanced Composition Explorer; IPS = interplanetary scintillation.

situation compared with the UCSD archival analysis. UCSD has maintained a forecast system since early in this century and has continued to update these analyses as improvements of the original technique are developed. Since mid-2016 the UCSD near real-time forecasts updated at a 6-hr cadence have also been archived online (at http://ips.ucsd.edu/high_resolution_predictions/). Since spring 2013, a near real-time forecast analysis has also been operated at the Korean Space Weather Center online (at http://www.spaceweather.go.kr/models/ips/).

The correlations between the CSSS modeled extrapolated fields and $B_z$ are a forward model from the IPS tomographic source surface, directly viewed in real-time below Earth, and vary with even lower resolution than the IPS velocities and densities. Thus, there is little reason to suggest that the forward model archival field predictions are much different from results when the system is used in a true forecast sense. We have operated a $B_z$ forecast at UCSD for over 2 years since the latter part of 2016 and have been gratified to find the $B_z$ forecast often indicates when enhanced geomagnetic activity will occur several days in advance. The Korean Space Weather Center has also recently provided this same $B_z$ modeling effort on the website (http://spaceweather.rra.go.kr/models/ipsace) as another way to provide inputs for their space weather forecasts. As an example of this ability we show one of the events from: Real-Time_Archive on the UCSD (http://ips.ucsd.edu/high_resolution_predictions/) website. At 21 UT 24 February 2017, a negative dip in the $B_z$ field component was forecast several days into the future (Figure 10a, see arrow), and indicated the value of $-B_z$ would tend toward a minimum on 28 February 2017. This forecast evolved over the next few days showing an even more pronounced and well-defined minimum beginning on 1 March 2017. The NOAA value of $B_z$ tracked the UCSD forecast well (Figure 10b), and in the middle of the final day following many days of little geomagnetic activity, the Kp index rose to 5 for several 3-hr intervals midday on 1 March 2017 (Figure 10c), and even higher the following day (not shown) indicating that a moderate geomagnetic storm was in progress. Enhancements of this effort have continued at UCSD, and in addition to time series plots, UCSD now provides volumetric data converted to GSM $B_z$ plotted like density and velocity as ecliptic, meridional, and Carrington plots at 1 AU (Figure 11). While not truly a valid concept except at Earth, the IPS analysis is better served in this way since this enables a forecaster to determine the nearness of the $-B_z$ value. Often, especially near solar minimum, the projected location of positive and negative RTN $B_t$ field that

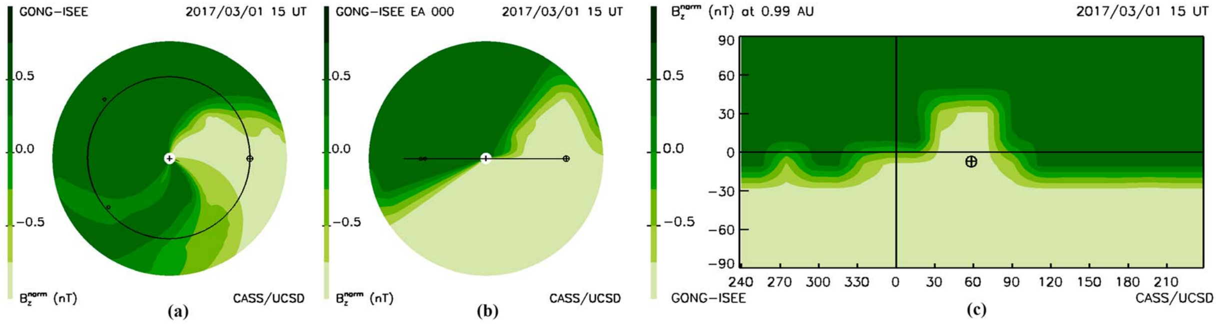


**Figure 11.** Geocentric Solar Magnetospheric $B_z$ field plotted as a volumetric prediction at the same time (1 March 2017 15 UT) as in Figure 10b. Values have been normalized to those present at 1 AU by removing a $r^{-1}$ falloff with solar distance. (a) as an ecliptic cut, (b) as a meridional cut that passes through Earth, and (c) as a Carrington map at the distance of the Earth (shown as "⊕" near the center of the plot). GONG = Global Oscillation Network Group; ISEE = Institute for Space-Earth Environmental Research.

provides the $B_z$ flux in these analyses can be almost a straight line centered on the heliographic equator. In these instances, slight latitude differences in the 3-D reconstructions can change the reversal location of the east-west field, and thus produce an uncertain forecast. The Figure 11 example indicates the presence of Earth where there is no doubt that the Earth has entered a region where $B_z$ is strongly negative.

To show the example in Figures 10 and 11 is not an isolated incident, we provide analyses from the whole 11-year data set by presenting a skill-score determination from our predicted data set. In this analysis we searched through our time series for a southward dip of GSM $B_z$ of at least 1.0 nT following a period with no negative $B_z$ of more than the 0.25 nT variation over 7 days prior. Of the 102 Carrington rotations studied with at least one $B_z$ decrease, there were 138 events of this type. For these we asked whether or not there was a minor or greater geomagnetic storm evidenced in the NOAA planetary Kp index within 1 day prior, or 2 days following the minimum of the change. These amplitudes and the threshold window were chosen because we have maximized comparisons of extrapolated fields to a 3-day boxcar average of the in situ measured magnetic field, and a quick pass through the our existing forecast archive to find the most likely set of best thresholds to use. If a geomagnetic storm occurred within this window, we consider this a positive result or a predicted $B_z$ change with an associated storm and thus an observed "hit." Following an equally weighted $2 \times 2$ contingency table as in Mozer and Briggs (2003), we found 77 three-day intervals where we correctly saw a storm ($n_{11}$); 62 predicted $B_z$ changes, with unobserved storms ($n_{01}$); 116 intervals where no negative $B_z$ was predicted, but a storm was observed ($n_{10}$); and 656 intervals where no $B_z$ decrease was predicted, and no storm was observed ($n_{00}$). As in Mozer and Briggs we determine a hit rate $H = (n_{11} + n_{00})/n) = 0.80$, where 1 is a perfect score and 0 is the worst possible. The threat score $TS = n_{11}/(n_{11} + n_{01} + n_{10}) = 0.30$ where again 1 is perfect and 0 the worst possible. The Probably of Detection $POD = n_{11}/(n_{11} + n_{01}) = 0.55$, where a perfect score is 1. The false-alarm rate $FAR = n_{01}/(n_{01} + n_{11}) = 0.40$, where the best possible score is 0 and the worst is 1. A global measure of the system is given by the bias, $B = (n_{11} + n_{01})/(n_{11} + n_{10}) = 0.72$, which implies that we are consistently not predicting all of the events present.

Although we used the archival data set to provide the 11-year skill-score analysis, we have retained a real-time archive of our forecasts from late October 2016 through to the present. The 11-year study in this article ended in May 2018. During this period we found 27 incidents of isolated geomagnetic storms and 16 locations where events were forecast at least 2 days in advance using the criterion established for our archival study. Although not all 16 forecasts resulted in a minor to moderate geomagnetic storm (three did not), we found only two forecast exceptions to the archived study. In one event on 8 November 2017 a forecast outage on our website prevented an event forecast several days in advance that was correctly predicted in the archive. For another storm on 20 April 2018 our forecast archive provided at least a 2-day forecast of this event even though the archival data set did not. Although this check covers only a portion of the of the time period as a true forecast, it is good to know for this study that the archived and forecast $B_z$ values agree as well as they do.

A hit rate of 0.80, or the knowledge of whether or not there will be a minor or greater storm within our allotted window of 1 day prior or 2 days following a predicted $B_z$ decrease is an excellent score. If we were to decrease the window over which we expected a storm to occur, the hit rate would be lower, the false alarm rate (now 0.40) would go higher, and the probability of detection (now 0.55) would also be lower. The probability of detection is related to the requirement that at least a minor storm must occur to provide a hit. The probability of detection is not as good as it will be in an operational setting since this score is dominated by the number of storms we did not predict that were associated with CMEs. In looking at the individual numbers by Carrington rotation, the values of $n_{10}$ are dominated by higher values of this in the time in 2015 during the declining phase of the last sunspot cycle where there are sometimes as many as four minor storms or greater observed that we did not predict. We often find in a failed prediction that a decreased $B_z$ provides an enhancement of geomagnetic activity but no minor storm. This is of course better captured by the Pearson's *R* correlations for a given Carrington rotation where no transient fields such as those from CMEs are present. The arrival of CMEs, as they are now, will presumably also be forecast at space weather centers using the techniques they currently have at hand, and with this knowledge, the success rate at the center for this type of forecast should be considerably greater.

## 7. Conclusions

We give specific examples of the UCSD archival and near real-time extrapolations using our IPS analysis and show a way that predicts daily changes in GSM $B_z$ component values at Earth. UCSD uses its IPS 3-D reconstruction model to extrapolate CSSS radial magnetic fields (Zhao & Hoeksema, 1995) to provide the timing and interactions present at 1 AU (see Jackson et al., 2016). Even though the resolution of the UCSD IPS 3-D reconstruction is low and limited primarily by the numbers of radio sources that can be observed in the sky by ISEE, these background analyses provide modeled values that are sufficiently accurate for a useful prediction. We show that there is a high correlation between the daily GSM component values $B_x$, $B_y$, and $B_z$ predicted by UCSD, and those provided by NOAA in our study that spans over the 11 years of extant GONG data. Although the general component correlation has been described before (Russell & McPherron, 1973), it is usually related to seasonal variations in geomagnetic activity, and not as much to changes in daily geomagnetic indices as shown in Figures 7, 8, and 10. UCSD has provided a near real-time forecast of the GSM component value using this technique since late 2016, and updates these every 6 hr on its website. Improvements to this technique have continued during this interval (Figure 11) to give an indication of the degree to which $B_z$ will become negative. The negative GSM $B_z$ field predictions we make daily should be used along with other information at a space weather center to provide a several-day advance forecasts of impending geomagnetic storms. In particular, CMEs are not thought present to a significant extent in our low-resolution magnetic field predictions, and a space weather center often has a far better capability of knowing when these will occur. Knowing that a CME is on its way can indicate that a large geomagnetic storm might occur within a short time range even though our current low-resolution field predictions give no indication of this.

A hit rate of 80%, or knowing within 1 day prior or 2 days following the predicted $B_z$ decrease that a minor or greater geomagnetic storm will occur, is an excellent score. We do not expect the hit rate to vary much in a true forecast situation since the field values are forward-models from near the solar surface and known and updated well in advance of their arrival at Earth. We have tested this from archives of real-time analyses over the last few years we have available, and found little difference between the forecast and archived data set. As we have shown, our prediction is somewhat better during solar minimum when there are fewer large transient events such as CMEs in the record. Studies show (e.g., Choi et al., 2017; Tsurutani et al., 2006), while CMEs may generally be responsible for the largest geomagnetic storms, that most geomagnetic storms and substorms have no discernable associated CME. The rather large window of 1 day prior and 2 days following the $B_z$ magnetic field decrease in the skill-score presentation is mostly dominated by the low-resolution of our CSSS model extrapolation technique. We find that with continual 6-hr updates, the prediction time of the exact $B_z$ decrease often becomes better known, and this refinement is not captured in the current prediction window for skill-scores we use at the end of section 6. The threshold values and window used in the skill-score analyses go in hand with the various averaging values used in our analyses, and indeed the quality and quantity of the data. These are expected to change in the future as other IPS data sets and different magnetic field extrapolation techniques become available, and when they do we expect to revisit this in a more thorough way.

It is well known that among other solar wind features, solar wind density and velocity are also factors associated with geomagnetic storm activity (Newell et al., 2007). Undoubtedly these other factors play an important role, and this is one of the major reasons the UCSD forecast page also predicts velocity; its increase can enhance the response at Earth of the effect of a GSM $B_z$ decrease and thus increase geomagnetic storm strength. A high velocity forecast just prior to the $B_z$ decrease can also be observed to shorten the arrival time of the decrease in the last day or two of the forecast. Future efforts in this work to provide better arrival times and nonradial transport of the fields causing these effects are currently one of the main efforts pursued by the UCSD IPS analysis effort (Jackson et al., 2015, 2016). We leave for the future effort a forecast of geomagnetic minor and moderate storm activity using the UCSD predicted parameter values in addition to the $B_z$ decrease to better quantify the effect of geomagnetic storm activity.

It was surprising to us that such a relatively small variation from a positive to negative GSM $B_z$ component field could provide as pronounced a result as we have found. We presume that part of the reason for this is simply that the low-resolution decreases we predict do not indicate the full negative shorter-lasting variations of field responsible for the triggering of minor and moderate geomagnetic storm activity. Proof of this idea, and whether this is the major reason for the effect we have found, is however beyond the scope of the current study.

**Acknowledgments**
The KSWC initiated and have supported this project in the past with partial funding to B. V. Jackson. In addition, B. V. Jackson, H. -S. Yu, and A. Buffington have been partially funded by AFOSR contract FA9550-11-1-0324 and past National Science Foundation (NSF) contracts AGS-1053766 and AGS-1358399 to the University of California, San Diego. B. V. Jackson and H. -S. Yu gratefully acknowledge the initial KSWC staff encouragement and seed money funding that led us to this discovery. The ISEE IPS observations were carried out under the solar wind program of the Solar-Terrestrial Environment Laboratory (STEL) of Nagoya University. The STELab near real-time IPS observations used in these analyses are available online (at ftp://ftp.stelab.nagoya-u.ac.jp/pub/vlist/rt/). We thank the ACE spacecraft group for making their data available in real time for use at UCSD through the Space Weather Prediction Center, NOAA, Boulder, Colorado (at http://www.swpc.noaa.gov/ftpdir/lists/ace2/). Global Oscillation Network Group (GONG) observations (http://gong.nso.edu/data/magmap/) of photospheric magnetic field are extrapolated outward from the Sun and used in both these archival and in the UCSD near real-time predictions. A special thanks is warranted for the SOHO/CELIAS data made available to UCSD in near real time by the Proton Monitor group at the University of Maryland, College Park, Maryland (at ftp://space.umd.edu/pm/houraverages.txt). Many of the images used in this article are available online, along with additional analyses and predictions, at the UCSD websites (http://ips.ucsd.edu, and http://ips.ucsd.edu/high_resolution_predictions).

## References

Ananthakrishnan, S., Coles, W. A., & Kaufman, J. J. (1980). Microturbulence in solar wind streams. *Journal of Geophysical Research*, *85*(A11), 6025. https://doi.org/10.1029/JA085iA11p06025

Behannon, K. W., Burlaga, L. F., & Hewish, A. (1991). Structure and evolution of compound streams at ≤ 1 AU. *Journal of Geophysical Research*, *96*(A12), 21213. https://doi.org/10.1029/91JA02267

Choi, K.-E., Lee, D.-Y., Choi, K.-C., & Kim, J. (2017). Statistical properties and geoeffectiveness of southward interplanetary magnetic field with emphasis on weakly southward $B_z$ events. *Journal of Geophysical Research: Space Physics*, *122*, 4921–4934. https://doi.org/10.1002/2016JA023836

Domingo, V., Fleck, B., & Poland, A. I. (1995). SOHO: The solar and heliospheric observatory. *Space Science Reviews*, *72*(1-2), 81–84.

Dunn, T., Jackson, B. J., Hick, P. P., Buffington, A., & Zhao, X. P. (2005). Comparative analyses of the CSSS calculation in the UCSD tomographic solar observations. *Solar Physics*, *227*(2), 339–353.

Gapper, G. R., Hewish, A., Purvis, A., & Duffet-Smith, P. J. (1982). Observing interplanetary disturbances from the ground. *Nature*, *296*(5858), 633–636.

Hewish, A., & Bravo, S. (1986). The sources of large-scale heliospheric disturbances. *Solar Physics*, *106*(1), 185–200.

Hewish, A., Scott, P. F., & Wills, D. (1964). Interplanetary scintillation of small diameter radio sources. *Nature*, *203*(4951), 1214–1217.

Houminer, Z. (1971). Correlation of interplanetary scintillation and spacecraft plasma density measurements. *Nature Physical Sciences*, *231*(25), 165–167.

Hovestadt, D., Hilchenbach, M., Bürgi, A., Klecker, B., Laeverenz, P., Scholer, M., et al. (1995). CELIAS—charge, element and isotope analysis system for SOHO. *Solar Physics*, *162*(1-2), 441–481. https://doi.org/10.1007/BF00733436

Jackson, B. V., Clover, J. M., Hick, P. P., Buffington, A., Bisi, M. M., & Tokumaru, M. (2013). Inclusion of real-time in-situ measurements into the UCSD time-dependent tomography and its use as a forecast algorithm. *Solar Physics*, *285*(1-2), 151–165.

Jackson, B. V., Hick, P. L., Kojima, M., & Yokobe, A. (1998). Heliospheric tomography using interplanetary scintillation observations 1. Combined Nagoya and Cambridge data. *Journal of Geophysical Research*, *103*(A6), 12,049–12,067. https://doi.org/10.1029/97JA02528

Jackson, B. V., & Hick, P. P. (2005). Three-dimensional tomography of interplanetary disturbances. In D. E. Gary & C. U. Keller (Eds.), *Solar and space weather radiophysics, current status and future developments, astrophysics and space science library* (Vol. 314, Chap. 17, pp. 355–386). Dordrecht, The Netherlands: Kluwer Academic.

Jackson, B. V., Hick, P. P., Bisi, M. M., Clover, J. M., & Buffington, A. (2010). Inclusion of in-situ velocity measurements in the UCSD time-dependent tomography to constrain and better-forecast remote-sensing observations. *Solar Physics*, *265*(1-2), 245–256. https://doi.org/10.1007/s11207-010-9529-0

Jackson, B. V., Hick, P. P., Buffington, A., Bisi, M. M., Clover, J. M., & Tokumaru, M. (2008). Solar mass ejection imager (SMEI) and interplanetary scintillation (IPS) 3D-reconstructions of the inner heliosphere. *Advances in Geosciences*, *21*, 339.

Jackson, B. V., Hick, P. P., Buffington, A., Bisi, M. M., Clover, J. M., Tokumaru, M., et al. (2011). Three-dimensional reconstruction of heliospheric structure using iterative tomography: A review. *Journal of Atmospheric and Solar - Terrestrial Physics*, *73*(10), 1214–1227.

Jackson, B. V., Hick, P. P., Buffington, A., Clover, J. M., & Tokumaru, M. (2012). Forecasting transient heliospheric solar wind parameters at the locations of the inner planets. *Advances in Geosciences*, *30*, 93.

Jackson, B. V., Hick, P. P., Buffington, A., Kojima, M., Tokumaru, M., Fujiki, K., et al. (2003). Time-dependent tomography of heliospheric features using interplanetary scintillation (IPS) remote-sensing observations. In M. Velli, R. Bruno, & F. Malara (Eds.), *Solar wind ten* (Vol. *679*, session I, pp. 75–78). Melville, New York.

Jackson, B. V., Hick, P. P., Buffington, A., Yu, H.-S., Bisi, M. M., Tokumaru, M., & Zhao, X. (2015). A determination of the north-south heliospheric magnetic field component from solar coronal closed-loop propagation. *Astrophysical Journal Letters*, *803*(L1), 1–5. https://doi.org/10.1088/2041-8205/803/1/L1

Jackson, B. V., Yu, H.-S., Buffington, A., Hick, P. P., Nishimura, N., Nozaki, N., et al. (2016). Exploration of solar photospheric magnetic field data sets using the UCSD tomography. *Space Weather*, *14*, 1107–1124. https://doi.org/10.1002/2016SW001481

Jian, L. K., MacNeice, P. J., Mays, M. L., Taktakishvili, A., Odstrcil, D., Jackson, B., et al. (2016). Validation for global solar wind prediction using Ulysses comparison: Multiple coronal and heliospheric models installed at the community coordinated modeling center. *Space Weather*, *14*, 592–611. https://doi.org/10.1002/2016SW001435

Jian, L. K., MacNeice, P. J., Taktakishvili, A., Odstrcil, D., Jackson, B., Yu, H.-S., et al. (2015). Validation for solar wind prediction at earth: Comparison of coronal and heliospheric models installed at the CCMC. *Space Weather*, *13*, 316–338. https://doi.org/10.1002/2015SW001174

Kamide, Y., McPherron, R. L., Gonzalez, W. D., Hamilton, D. C., Hudson, H. S., Joselyn, J. A., et al. (1997). In B. T. Tsurutani, W. D. Gonzalez, Y. Kamide, & J. K. Arballo (Eds.), *Magnetic storms: Current understanding and outstanding questions*, *Geophysical Monograph Series* (p. 1). Washington, DC: American Geophysics Union.

Kojima, M., & Kakinuma, T. (1987). Solar cycle evolution of solar wind speed structure between 1973 and 1985 observed with the interplanetary scintillation method. *Journal of Geophysical Research*, *92*(A7), 7269. https://doi.org/10.1029/JA092iA07p07269

Kojima, M., Tokumaru, M., Watanabe, H., Yokobe, A., Asai, K., Jackson, B. V., & Hick, P. L. (1998). Heliospheric tomography using interplanetary scintillation observations 2. Latitude and heliocentric distance dependence of solar wind structure at 0.1–1 AU. *Journal of Geophysical Research*, *103*(A2), 1981–1989. https://doi.org/10.1029/97JA02162

Linker, J. A., Caplan, R. M., Downs, C., Riley, P., Mikic, Z., Lionello, R., et al. (2017). The open flux problem. *Astrophysical Journal Letters*, *848*(1), 70.

MacNeice, P., Jian, L., Antiochos, S. K., Arge, C. N., Bussy-Virat, C. D., DeRosa, M. L., et al. (2018). Assessing the quality of models of the ambient solar wind. *Space Weather*, *16*, 1644–1667. https://doi.org/10.1029/2018SW002040

McComas, D. J., Bame, S. J., Barker, P., Feldman, W. C., Phillips, J. L., Riley, P., & Griffee, J. W. (1998). Solar wind Electron proton alpha monitor (SWEPAM) for the advanced composition explorer. *Space Science Reviews*, *86*(1/4), 563–612.

Mozer, J. B., & Briggs, W. M. (2003). Skill in real-time solar wind shock forecasts. *Journal of Geophysical Research*, *108*(A6), 1262. https://doi.org/10.1029/2003JA009827

Newell, P. T., Sotirelis, T., Liou, K., Meng, C.-I., & Rich, F. J. (2007). A nearly universal solar wind-magnetosphere coupling function inferred from 10 magnetospheric state variables. *Journal of Geophysical Research*, *112*, A01206. https://doi.org/10.1029/2006JA012015

Ogilvie, K. W., & Parks, G. K. (1996). First results from WIND spacecraft: An introduction. *Geophysical Research Letters*, *23*(10), 1179–1181. https://doi.org/10.1029/96GL01357

Parker, E. N. (1958). Dynamics of the interplanetary gas and magnetic fields. *The Astrophysical Journal*, *128*, 664.

Russell, C. T. (2001). Solar wind and interplanetary magnetic field: A tutorial. In P. Song, H. J. Singer, & G. L. Siscoe (Eds.), *Space weather*, *Geophysical Monograph Series* (Vol. 125, section II, pp. 73–89). Washington, DC: American Geophysical Union.

Russell, C. T., & McPherron, R. L. (1973). Semiannual variation of geomagnetic activity. *Journal of Geophysical Research*, *78*(1), 92–108. https://doi.org/10.1029/JA078i001p00092

Stone, E. C., Frandsen, A. M., Mewaldt, R. A., Christian, E. R., Margolies, D., Ormes, J. F., & Snow, F. (1998). The advanced composition explorer. *Space Science Reviews*, *86*(1/4), 1–22.

Tokumaru, M. (2013). Three-dimensional exploration of the solar wind using observations of interplanetary scintillation. *Proceedings of the Japan Academy. Series B, Physical and Biological Sciences*, *89*(2), 67–79.

Tokumaru, M., Kojima, M., Fujiki, K., Maruyama, K., Maruyama, Y., Ito, H., & Iju, T. (2011). A newly developed UHF radiotelescope for interplanetary scintillation observations: Solar wind imaging facility. *Radio Science*, *46*, RS0F02. https://doi.org/10.1029/2011RS004694

Tsurutani, B. T., Gonzalez, W. D., Gonzalez, A. L. C., Guarnieri, F. L., Gopalswamy, N., Grande, M., et al. (2006). Corotating solar wind streams and recurrent geomagnetic activity: A review. *Journal of Geophysical Research*, *111*, A07S01. https://doi.org/10.1029/2005JA011273

Zhao, X., & Hoeksema, J. T. (1995). Prediction of the interplanetary magnetic field strength. *Journal of Geophysical Research*, *100*(A1), 19. https://doi.org/10.1029/94JA02266